International Journal of Multiphase Flow 94 (2017) 107–122

Contents lists available at ScienceDirect

International Journal of Multiphase Flow

journal homepage: www.elsevier.com/locate/ijmulflow

Characterization of drop aerodynamic fragmentation in the bag and sheet-thinning regimes by crossed-beam, two-view, digital in-line holography

Daniel R. Guildenbecher[a,*], Jian Gao[b], Jun Chen[c], Paul E. Sojka[c]

[a] Sandia National Laboratories, Albuquerque, NM, USA
[b] Department of Mechanical Engineering, Johns Hopkins University, Baltimore, MD, USA
[c] School of Mechanical Engineering, Purdue University, West Lafayette, IN, USA

ARTICLE INFO

Article history:
Received 21 July 2016
Revised 1 February 2017
Accepted 18 April 2017
Available online 19 April 2017

ABSTRACT

When a spherical liquid drop is subjected to a step change in relative gas velocity, aerodynamic forces lead to drop deformation and possible breakup into a number of secondary fragments. To investigate this flow, a digital in-line holography (DIH) diagnostic is proposed which enables rapid quantification of spatial statistics with limited experimental repetition. To overcome the high uncertainty in the depth direction experienced in previous applications of DIH, a crossed-beam, two-view configuration is introduced. With appropriate calibration, this diagnostic is shown to provide accurate quantification of fragment sizes, three-dimensional positions and three-component velocities in a large measurement volume. These capabilities are applied to investigate the aerodynamic breakup of drops at two non-dimensional Weber numbers, *We*, corresponding to the bag ($We = 14$) and sheet-thinning ($We = 55$) regimes. Ensemble average results show the evolution of fragment size and velocity statistics during the course of breakup. Results indicate that mean fragment sizes increase throughout the course of breakup. For the bag breakup case, the evolution of a multi-mode fragment size probability density is observed. This is attributed to separate fragmentation mechanisms for the bag and rim structures. In contrast, for the sheet-thinning case, the fragment size probability density shows only one distinct peak indicating a single fragmentation mechanism. Compared to previous related investigations of this flow, many orders of magnitude more fragments are measured per condition, resulting in a significant improvement in data fidelity. For this reason, this experimental dataset is likely to provide new opportunities for detailed validation of analytic and computational models of this flow.

1. Introduction

1.1. Aerodynamic fragmentation of drops

It is well known that a liquid drop moving through a surrounding gas with non-zero relative velocity will experience some form of deformation. This is due to the competition between aerodynamic drag, which applies a non-uniform stress to the drop surface, and interfacial tension, which attempts to counteract that stress distribution. If the former is sufficiently greater than the latter, the drop may be deformed to the point of fragmentation. This is illustrated in Fig. 1, which shows typical experimental images of the breakup process. Due to the inclusion of interfacial as well as internal and external flow physics, an initial geometry that lends itself to experimental, analytical and computational investigation, and applicability to many spray processes, the aerodynamic fragmentation of a drop has become something of a canonical flow problem. As such, it has been studied for decades with a number of recent review articles (Pilch and Erdman, 1987; Guildenbecher et al., 2009; Theofanous, 2011).

In a typical spray application, a liquid is injected from a nozzle forming a jet which undergoes primary atomization into droplets. Following that, droplets may further fragment due to interactions with the gas. Because the aerodynamic breakup of droplets follows primary atomization in time, the process studied here is also sometimes referred to as secondary breakup or secondary atomization (Guildenbecher et al., 2009).

Years of investigation has led to the general conclusion that the most relevant non-dimensional parameter is the Weber number, which quantifies the ratio of disruptive aerodynamic forces to

* Corresponding author.
E-mail address: drguild@sandia.gov (D.R. Guildenbecher).

http://dx.doi.org/10.1016/j.ijmultiphaseflow.2017.04.011
0301-9322/

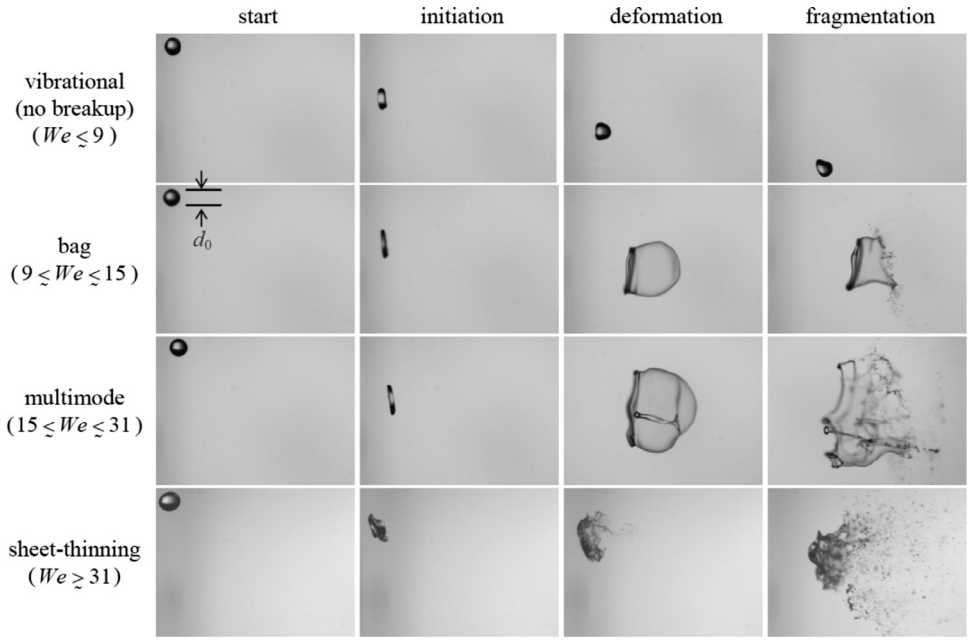

Fig. 1. Ethanol drops undergoing aerodynamic fragmentation. Images are from Guildenbecher and Sojka (2011) and were acquired using the same experimental facility discussed here. Time increased from left to right, relative gas velocity increases from top to bottom.

restorative surface tension forces,

$$We = \rho_g d_0 u_0^2 / \sigma. \quad (1)$$

Here, ρ_g is the gas-phase density; d_0 is the initial spherical drop diameter; u_0 is relative velocity; and σ is the interfacial surface tension. As *We* increases, various flow morphologies are observed as illustrated in Fig. 1. These morphological differences have motivated many investigations of the underlying flow physics, and, despite decades of work, much debate remains as to the instability mechanisms which presumably determine the flow morphologies (Theofanous, 2011).

In addition to *We*, viscous effects can be accounted for with the non-dimensional Ohnesorge number, $Oh = \mu_l / \sqrt{\rho_l d_0 \sigma}$, where μ_l and ρ_l are the drop viscosity and density, respectively. As *Oh* increases, viscous effects tend to retard deformation and breakup. Still, when $Oh \lesssim 0.1$ viscous effects are generally thought to be negligible (Hsiang and Faeth, 1992). Such is the case for the experimental results presented here. For this reason viscous effects are not considered further in this work.

Despite the general interest in flow morphologies and viscous effects, these are not always the most important quantities of interest. Rather for combustion applications, the size and velocity of the fragments produced by the breakup process are often most critical due to the strong effect these values have on dispersion, evaporation, and reaction rates. For this reason, significant modeling efforts have focused on prediction of fragment sizes and velocities. Early analytical work (the TAB model of O'Rourke and Amsden (1987) and perhaps as far back as GI Taylor (1950; 1963) and Lamb (1916)) used force or energy concepts to derive simplified models for drop deformation. By assuming a critical deformation which leads to breakup, fragment sizes and velocities were predicted. Later efforts by Sellens and Brzustowski (1985) and Li and Tankin (1987) employed Shannon-like entropy maximization approaches to derive analytic estimates of the fragment size and velocity probability density functions (*pdf*). These and related models form the basis of many spray simulation methods (Reitz, 1987). For more detailed investigation of flow physics, numerical investigations have been performed which solve the multiphase Navier–Stokes equations including interfacial tension. The first such investigation may be that of Masliyah and Epstein (1970), who studied the deformation of axisymmetric oblate and prolate spheroid flows at low Reynolds numbers. In the subsequent years, a number of groups have considered some combination of non-isothermal, deforming, unsteady, viscous, and/or evaporating cases. Examples include studies by Tryggvason and co-workers (Tryggvason, 1997; Han and Tryggvason, 1999, 2001), Quan and co-workers (Quan and Schmidt, 2006; Quan et al., 2009a; Quan et al., 2009b), Wadhwa et al. (2005, 2007), and, most recently, Kekesi et al. (2014). Much of these studies focused on simulating drop deformation before breakup; however, recent progress has been made using level set and volume of fluid methods (Gorokhovski and Herrmann, 2008) to simulate aerodynamic fragmentation of liquid jets in cross-flows and other related geometries (Desjardins et al., 2008; Herrmann, 2010; Arienti et al., 2013). These interface capturing methods have sometimes been referred to as "direct numerical simulation" of atomization; however, due to the immense range of length scales (possibly including pinch off of fragments at nanometer scales Arienti et al. (2011) the predicted fragment sizes and velocities remain grid dependent (Herrmann, 2010; Arienti et al., 2013).

From this brief review it is clear that there are many existing and emerging modeling techniques for the prediction of fragment sizes and velocities from the aerodynamic breakup of liquid drops. All of these techniques require some modeling assumptions which should be experimentally verified. However, due to limitations of available diagnostics, many of the previous experimental results have been restricted to qualitative imaging, similar to Fig. 1, along with limited quantitative information on drop deformation. Only a few studies have attempted to quantify fragment sizes and velocities using point-wise phase Doppler anemometry (PDA) (Kulkarni et al., 2012) or analog holography (Hsiang and Faeth, 1992, 1993, 1995; Hwang et al., 1996; Chou et al., 1997; Chou and Faeth, 1998; Dai and Faeth, 2001). Consequently datasets remain sparse, and many of the existing models have yet to be fully validated.

1.2. Digital in-line holography (DIH)

In Gao et al. (2013b) we proposed the use of digital inline holography (DIH) for investigation of this flow. In DIH a collimated

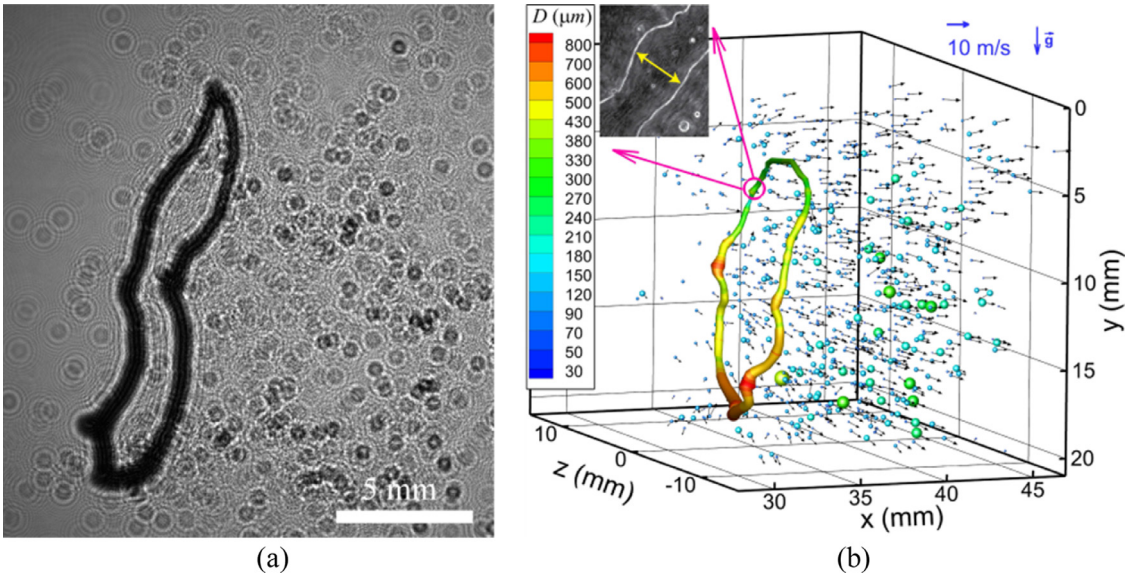

Fig. 2. Example DIH results for the breakup of an ethanol drop in an air-stream from Gao et al. (2013b). (a) Experimental hologram and (b) the 3D-3C particle field measured from this hologram pair.

laser beam is passed through a particle field. Resulting diffraction patterns are recorded using a digital sensor (CCD or CMOS). By solving the diffraction integral equations, the recorded hologram is numerically refocused along the optical depth revealing images of the particles at their original three-dimensional (3D) locations (Katz and Sheng, 2010). With appropriately defined image processing methods (Gao et al., 2013a, 2014a; Guildenbecher et al., 2013), particle positions, sizes, and in-plane morphologies can be automatically measured from the refocused images. Finally, by recording more than one hologram in quick succession, frame-to-frame matching can be used to determine three-component (3C) particle velocities. For example, Fig. 2(a) shows a digital hologram of the breakup of an ethanol drop in an air stream recorded at a time when the bag structure shown in the second row in Fig. 1 has fragmented yet the ring remains intact (Gao et al., 2013b). Using the methods described in Gao et al. (2013b), this hologram was processed to quantify the 3D-3C results shown in Fig. 2(b).

Fig. 2 illustrates a number of advantages of DIH for quantification of this flow: (1) Hundreds of particles can be measured from a single realization. In comparison to point measurement techniques such as PDA (Kulkarni et al., 2012), this greatly improves our ability to measure statically converged particle size distributions with limited experimental repetition. (2) Unlike PDA, DIH can quantify highly non-spherical particles, as illustrated by the measured ring structure shown in Fig. 2(b). As a consequence, measurements can be performed at the site of breakup where many non-spherical structures persist. This may be particularly advantageous for validation of emerging interface capturing simulations which predict similar flow structures (Desjardins et al., 2008; Gorokhovski and Herrmann, 2008; Herrmann, 2010; Arienti et al., 2013). (3) The use of digital sensors and numerical reconstruction significantly increases the rate at which data can be acquired and processed when compared to traditional analog holography, which required photographic plates and tedious optical reconstruction (Hsiang and Faeth, 1992, 1993, 1995; Hwang et al., 1996; Chou et al., 1997; Chou and Faeth, 1998; Dai and Faeth, 2001). Consequently, more conditions can be practically investigated in the time constraints of a single experiment.

In addition, DIH has some important challenges: (1) Due to the overlap of particle images, the method is limited in its ability to study dense particle fields. The particle fields investigated here are relatively sparse and this is not a significant challenge in the current work; however, this is likely to be a significant challenge if DIH is considered for study of the optically dense sprays often encountered in industrial applications (Linne, 2013). (2) At the current time data processing techniques are not commercially available and significant efforts are often required to develop custom data processing algorithms for specific applications. (3) Finally, and most important for the current investigation, DIH suffers from the depth-of-focus challenge discussed in Katz and Sheng (2010). Because particle depth is reconstructed from a limited angular aperture, there tends to be high uncertainty in the measured particle position along the optical depth. For 3C velocity measurements, this results in significantly higher velocity uncertainty in the depth direction compared to the two in-plane directions.

Here, we expand upon the initial DIH results presented in Gao et al. (2013b) by introducing a crossed-beam, two-view DIH configuration, which significantly reduces uncertainty in the depth direction. After quantifying this improvement, we proceed to investigate the size and velocity of fragments produced by breakup of an ethanol drop in an air-stream. Two flow morphologies are investigated (bag and sheet-thinning) at various times during the fragmentation process. This allows us to expand upon previous work (Gao et al., 2013b) by providing size-velocity statistics as a function of *We* and time.

All of the experiments performed here have been done using the same droplet generator and air nozzle utilized in a number of previous experiments (Guildenbecher and Sojka, 2011; Flock et al., 2012; Kulkarni et al., 2012; Gao et al., 2013b, 2014b, 2015; Kulkarni and Sojka, 2014). Most notably, the experimental conditions chosen here closely match those of Flock et al. (2012) who used video imaging to quantify initial trajectories and deformation rates of ethanol drops in a cross-flow. Together with the experimental results reported here, these data provide quantification of aerodynamic breakup from early time deformation to late time fragmentation with what we believe is unprecedented accuracy and quantified uncertainty. As such, these data will provide new opportunities for detailed model development and validation.

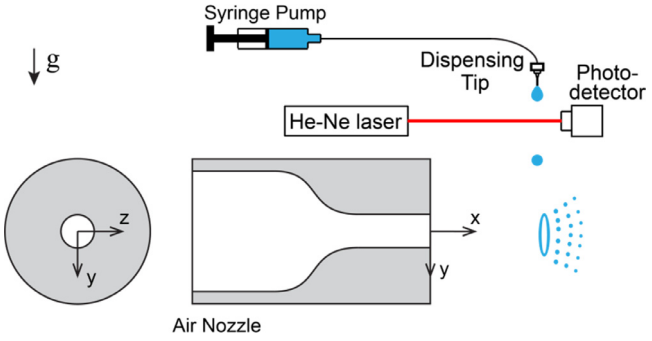

Fig. 3. Drop formation apparatus and air jet. A pictorial representation of bag breakup, showing bag and rim fragments, is included.

2. Methods

2.1. Experimental configuration

The experimental apparatus to investigate aerodynamic drop breakup is shown in Fig. 3. Single drops are generated by syringe pumping a liquid to a dispensing tip that is mounted above an air-nozzle. Measurements are initiated when a drop falls through a He-Ne laser beam and partially obstructs its signal to a photodetector. This supplies a trigger pulse to the laser and digital cameras, which record the breakup process. The time delay between the blocking of the He-Ne beam and the triggering of the laser and cameras can be altered to investigate different phases of the breakup process. Furthermore, since the air-nozzle and dispensing tip are mounted on an *x*-*y* traversing system they can be translated so that the camera fields of view are centered at the desired locations relative to the air-nozzle.

As was done in Flock et al. (2012), all drops are formed using ethanol with assumed surface tension, $\sigma = 0.0244$ N/m, density, $\rho_l = 789$ kg/m^3, and viscosity, $\mu_l = 1.2 \times 10^{-3}$ Ns/m^2. Ethanol was chosen because it is readily available in high purity. In addition, since surface tension and viscosity are relatively low, conditions leading to fragmentation can be achieved with moderate gas-velocities, which are easily attained in the laboratory. Experiments are performed at Purdue University where atmospheric air has an approximate density, $\rho_g = 1.2$ kg/m^3. Multiple breakup conditions are investigated by altering the mass flow rate of air through the nozzle. This is quantified using a Coriolis mass flow meter (Micro Motion F-series) with manufacture specified precision of ±0.1%. Further details on the air-nozzle configuration including nozzle dimensions and measurements of the air-jet velocity field are available in Flock et al. (2012) and Guildenbecher (2009). Finally, experiments are performed indoors where the room air temperature and the initial temperature of the ethanol is approximately 22 °C. As discussed in Flock et al. (2012) evaporation of the core drop during the initial deformation phase is likely to be minimal. However, those interested in detailed modeling of the data reported here may need to consider the effects of evaporation on the relatively small secondary fragments.

To address the depth-of-focus problem, we choose to implement two simultaneous DIH measurements. This is motivated by previous work which has shown that multiple fields of view can be used to reduce the reliance on the numerically reconstructed particle depth in the final measurement of 3D particle positions (Lu et al., 2008; Soria and Atkinson, 2008; Buchmann et al., 2013; Tani et al., 2015). These previous works have typically employed orthogonal fields of view which eliminate the uncertainty introduced by the depth-of-focus problem. However, an orthogonal configuration also requires extensive optical access, negating the advantage of DIH for 3D measurement from a single line-of-sight. Because the current experimental facility does not allow for easy optical access for orthogonal fields-of-view, we chose instead to implement a two-view DIH configuration with a narrow stereo-angle between the fields of view. As discussed in this section (and in further detail in a few initial conference proceedings by Gao et al., 2014b, 2015), this crossed-beam, two-view DIH configuration has its own specific advantages and challenges.

The optical configuration is shown in Fig. 4. The beam from a double-pulsed Nd: YAG laser (532 nm, 8 ns pulse width) is divided into two. Each resulting beam is spatially filtered, expanded and collimated before illuminating the particle field. The origin of the global coordinate system (*x, y, z*) is at the center of the 25.4 mm diameter air-nozzle exit plane. The positive *x*-direction is along the air flow, and the positive *y*-direction is along gravity. Choice of this coordinate system means both beams are parallel to the *x*-*z* plane. One beam axis is aligned with the *z*-direction (beam 1), while the beam 2 axis is at a small angle, θ, with respect to beam 1.

The interference patterns produced by fragmenting drops are recorded using two identical CCD cameras (4008 × 2672 pixels, 9 × 9 μm pixel pitch), which are operated in double-exposure mode synchronized to the double laser pulses in the same manner as a particle image velocimetry (PIV) instrument. This results in sequential holograms recorded with known time separation, Δt. For the conditions considered here Δt varies between 16 and 33.5 μs. Sample holograms are presented in the top row of Fig. 5 where the same drop fragmentation is recorded from the two perspectives at the same instant in time.

2.2. Hologram processing to extract fragment positions and sizes

Here methods for numerical refocusing and automatic extraction of particle properties are discussed with reference to the view 1 coordinates. Data processing for the view 2 results is identical.

After recording, holograms are numerically refocused along the optical depth, z_1, by solving the diffraction integral equation,

$$E(x_1, y_1; z_1) = [I_0(x_1, y_1) E_r^*(x_1, y_1)] \otimes g(x_1, y_1; z_1), \quad (2)$$

Here, $E(x_1,y_1;z_1)$ is the reconstructed complex amplitude at optical depth, z_1; $I_0(x_1,y_1)$ is the recorded hologram; $E_r^*(x_1,y_1)$ is the conjugate reference wave (assumed constant for a plane wave); ⊗ is the convolution operation; and $g(x_1,y_1;z_1)$ is the diffraction kernel (Schnars and Jueptner, 2005; Katz and Sheng, 2010). Eq. (2) is numerically evaluated to find $E(x_1,y_1;z_1)$ at any z_1, and the reconstructed light field is visualized using its amplitude $A = |E|$.

The bottom row in Fig. 5 shows the amplitude images which are created when the holograms in the top row are numerically refocused using Eq. (2) to an optical depth corresponding to the approximate center of the particle field. Some of the fragments appear in-focus at this depth while others, which are located at different depths, are out-of-focus. For automatic extraction of the 3D position of all fragments, we utilize the data processing algorithms proposed in Guildenbecher et al. (2013) and Gao et al. (2013a, 2014a) and briefly summarized here. First, a hologram is numerically refocused through 2001 planes evenly spaced along the z_1-direction to create a projection of the minimum amplitude in the depth direction. This is thresholded using the global optimum threshold defined in Gao et al. (2013a) to determine an initial estimate of particle locations in the x_1-y_1 plane. Next, our hybrid refinement method (Guildenbecher et al., 2013) is applied to measure the particle depth based on the average z_1-location of maximum edge sharpness as calculated during the depth sweep. To further improve the measured in-plane particle sizes, a second hybrid refinement is performed using the reconstructed amplitude at each measured particle z_1-location. To minimize detection of false particles, measured regions with area equivalent diameter, *d*, less than three times the pixel size (27 μm) or greater than 2 mm are elim-

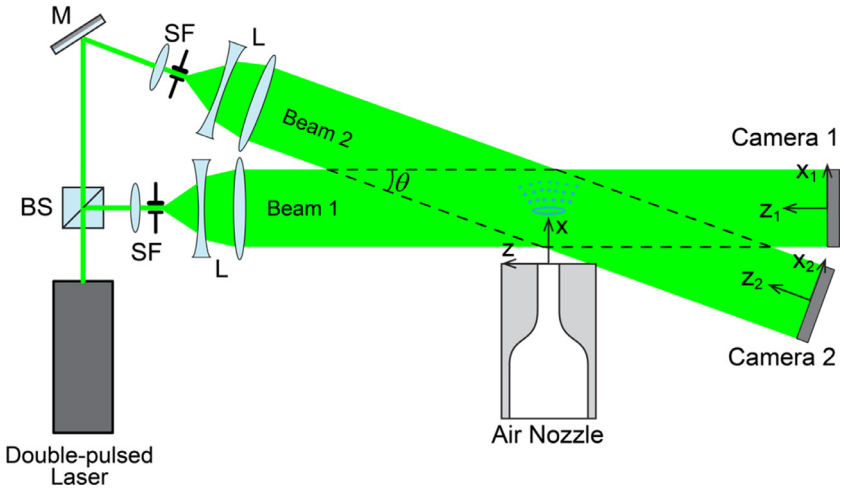

Fig. 4. Crossed-beam, two view DIH system. BS: 50–50 beam-splitter, M: mirror, SF: spatial filter, L: collimating lenses.

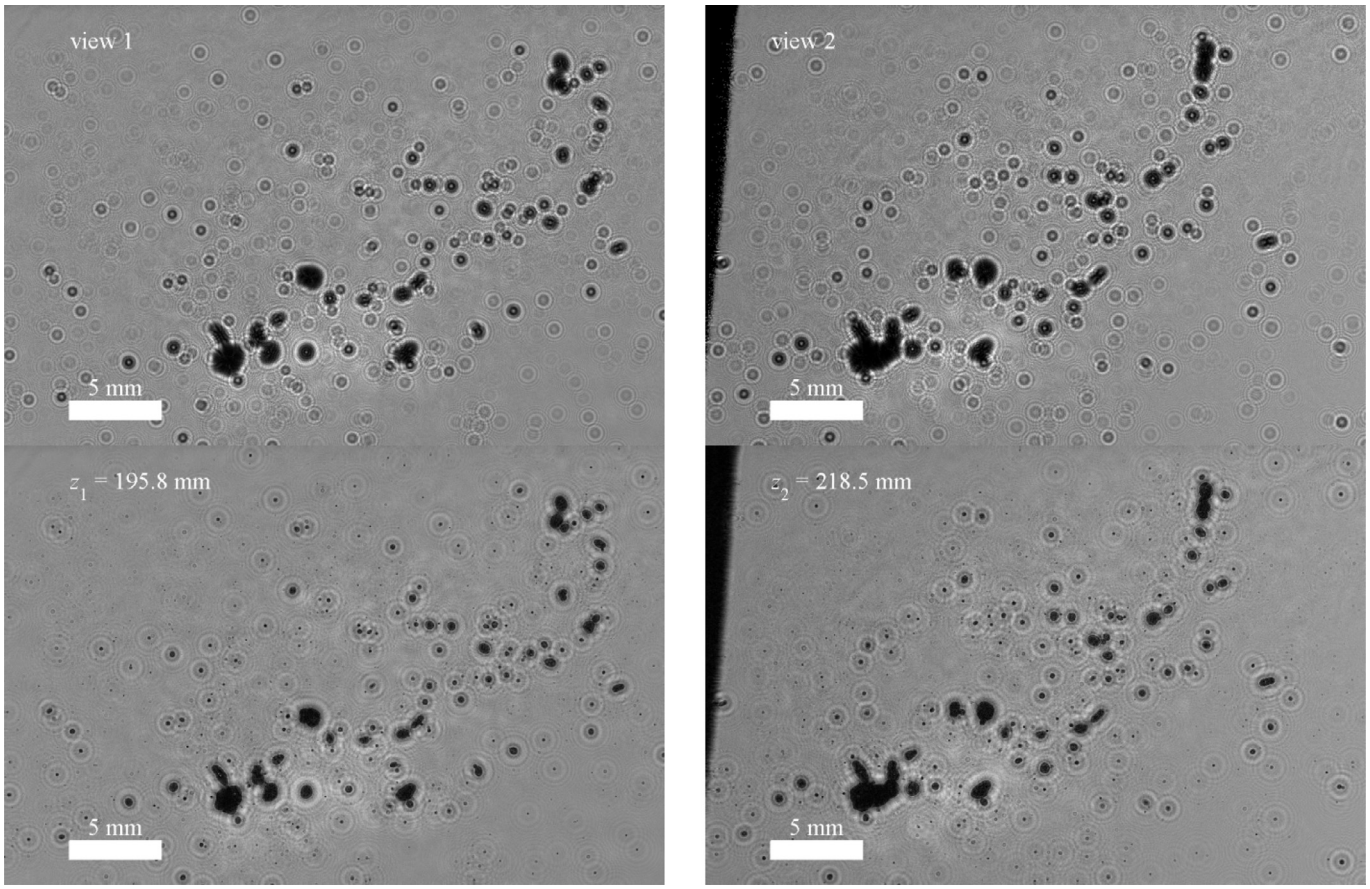

Fig. 5. (top row) Sample holograms recorded using the two views at the same instant in time, and (bottom row) amplitude images which have been numerically refocused using Eq. (2) to the optical depth shown.

inated. Finally, to determine velocities, fragments detected in sequential holograms are paired using the match probability method of Tinevez (2012). The subtraction of 3D coordinates yields displacements, which are then divided by Δt to compute 3C velocities.

Fig. 6(a) shows the results when the view 1 hologram in Fig. 5(a) is processed in this manner. The top image in Fig. 6(a) shows the amplitude images focused to the measured z_1-location of each drop. Colored circles show the measured d, and white arrows show the measured x_1-y_1 velocities. The ordinate in the middle image in Fig. 6(a) shows the measured particle positions in the depth direction (z_1), along with the corresponding velocities. Finally, the chart in the bottom of Fig. 6(a) shows the probability density of fragment size determined from the 754 fragments measured at this instance. (Note, processing of view 2 gives qualitatively similar results). The main flow is expected in the x_1-direction, yet significant scatter is observed in z_1-velocities. This is due to uncertainty introduced by the depth-of-focus problem (Katz and Sheng, 2010).

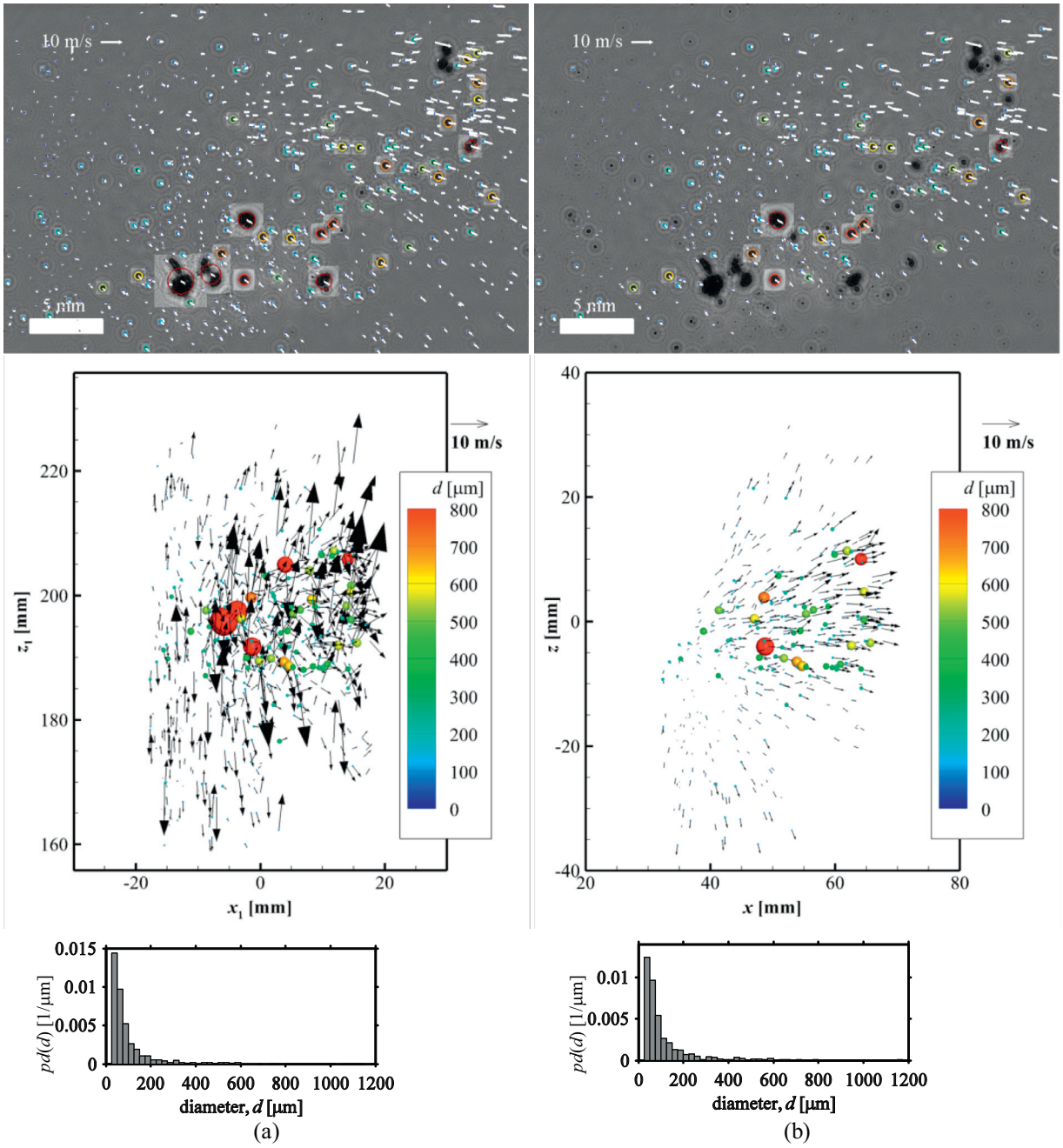

Fig. 6. 3D representation of typical fragment size and velocity fields: (a) velocity vectors and sizes obtained using view 1 of the single-view DIH configuration, and (b) velocity vectors and sizes obtained using the two-view DIH configuration. (top row) Measured in-plane sizes and velocities; background shows the recorded hologram numerically refocused to the approximate center of the breakup event, and bright squares show the particle images refocused to their measured z-locations. (middle row) Reconstructed top-down view of the breakup event. (bottom row) Number probability density, $pd(d)$. (For interpretation of the references to color in the text, the reader is referred to the web version of this article.)

To address this, we propose here to combine the view 1 and view 2 results as described in the next sub-sections.

2.3. Calibration of the crossed-beam configuration

Before processing the fragment data, it is necessary to find an accurate transformation between the measured view 1 and view 2 coordinates and the global (x, y, z) coordinates. Transformation of the (x_1, y_1, z_1) coordinates is trivial requiring only the subtraction of the z-offset (195.8 mm). The (x_2, y_2, z_2) coordinates are assumed to be related to the global (x, y, z) coordinates via the transformation matrix,

$$\begin{bmatrix} x \\ y \\ z \\ 1 \end{bmatrix} = \begin{bmatrix} \cos(\theta) & 0 & \sin(\theta) & C_x \\ 0 & 1 & 0 & C_y \\ -\sin(\theta) & 0 & \cos(\theta) & C_z \\ 0 & 0 & 0 & 1 \end{bmatrix} \begin{bmatrix} x_2 \\ y_2 \\ z_2 \\ 1 \end{bmatrix}, \tag{3}$$

where C_x, C_y, and C_z are translation offsets in the x-, y-, and z-directions, respectively, and θ is the aforementioned rotation offset between the two fields of view.

C_x, C_y, C_z, and θ are determined via the calibration procedure described in Gao et al. (2014b). An upright needle mounted on an x-z micrometer stage is translated within the field of view of both

Table 1
Coordinate transformation parameters obtained from calibration.

$\theta \pm \delta\theta = 0.335 \pm 0.002$ rad
$C_x \pm \delta C_x = -67.9 \pm 0.2$ mm
$C_y \pm \delta C_y = 0.47 \pm 0.02$ mm
$C_z \pm \delta C_z = -206.4 \pm 0.5$ mm

cameras. The recorded holograms are processed in a similar manner to that described previously. This yields a series of measured (x_1, y_1, z_1) and (x_2, y_2, z_2) coordinates along with known x-z displacements. By rearranging the system of equations in Eq (3), θ is first determined as a function of the measured quantities. Following this, the remaining equations are solved for C_x, C_y, and C_z.

Table 1 gives the measured results, where uncertainty is shown as the standard deviation from 16 measurements. Note, the measured θ is 19.1°, which is much smaller than the 90° beam crossing angle investigated previously (Lu et al., 2008; Buchmann et al., 2013; Tani et al., 2015). The advantage of a small θ is the increased detection volume (overlapping region of the two beams). In particular, the current detection volume is $3/\sin(\theta)$ times that of an orthogonal-view configuration when the same cameras are used. However, the small θ does not eliminate all uncertainties in out-of-plane direction. This must be properly accounted for in the fragment positional measurements, as discussed in the next subsection.

Finally, note that C_x in Table 1 does not include the additional offset caused when the air nozzle is translated away from the center of the view 1 field of view (see Fig. 4). This offset, which changes as the nozzle is moved to visualize different stages of the breakup process, is added after transformation to find the final x-positions reported in the remainder of this work.

2.4. Fragment measurements using the crossed-beam configuration

To determine the fragment correspondence between the views, measured fragment (x_1, y_1, z_1) and (x_2, y_2, z_2) positions are first transformed to the global (x, y, z) coordinates using the methods described in the previous section. Next, a nearest neighbor search is preformed to match the fragments between the two views. Matches are accepted with positional discrepancies less than 0.95 mm in the x-direction, 0.32 mm in the y-direction, and 1.35 mm in the z-direction. These criteria are selected based on the propagation of uncertainty analysis performed by Gao et al. (2014b) which uses the measured uncertainties in Table 1 to estimate the expected uncertainties in particle localization after coordinate transformations. In addition, particle matches with greater than 15% difference in measured area equivalent diameter, d, are eliminated.

Using propagation of uncertainties, it can be shown that the measured particle (x, y, z) positions from view 1 have lower uncertainty compared to the values measured from the transformation of view 2 coordinates or even the average of the view 1 and 2 results (Gao et al., 2014b). This can be understood by noting that the view 1 coordinates are aligned with the global coordinates and therefore the in-plane coordinates (x-y) do not suffer from any additional uncertainty introduced by the transformation (see Table 1). Interestingly, even the particle depth z, measured from view 1 alone is more accurate, despite the fact that it suffers from the depth-of-focus problem. As discussed further in Gao et al. (2014b), the value determined by the triangulation equation, $z=(x_1-C_x)\cot\theta - x_2\csc\theta + C_z$, which does not directly depend on any measure of out-of-plane coordinates (z_1 or z_2), still suffers from higher uncertainty due to the uncertainty of the calibration constants, which incorporates uncertainty introduced by the depth-of-focus problem during calibration. (Note: this would not be true for orthogonal fields of view which do not rely on reconstructed optical depth for calibration or measurements). For the reasons mentioned, the final 3D particle positions and x-y velocities are taken from the quantities measured from the view 1 coordinates.

Nevertheless, the crossed-beam, two-view configuration proposed here does have specific advantages. The top image in Fig. 6(b) shows the measured in-plane fragment sizes and positions after processing in this manner. Careful inspection of this figure reveals that the total number of measured fragments has decreased compared to the single view results shown in Fig. 6(a). This is partially caused by the reduction in the effective measurement volume, which is constrained to the overlap region shown by the diamond-shaped region enclosed by the dotted line in Fig. 4. In addition, the imposed size and position discrepancy limits tend to eliminate fragments which are poorly detected in one or both views. For example, the large regions in the lower left corner of the image in Fig. 6(a) wherein multiple overlapped particles are detected as one large particle have been eliminated from the measurement in Fig. 6(b). Without the crossed-beam configuration, errors of this nature cannot be easily detected or eliminated with automated data processing routines. We believe that this ability to filter false measurements is one of the important advantages of the two-view configuration.

Comparison of the size probability density from the single-view results in the bottom of Fig. 6(a) with the crossed-beam results in Fig. 6(b), indicates that data filtering in this manner has a minimal effect on the overall shape of the probability density. Indeed, the mean diameters measured with the single-view (106 μm) and the crossed-beam configuration (114 μm) differ by less than 8%. On the other hand, the few large fragments are much more likely to overlap other fragments within a single field-of-view. Because these large fragments make up a considerable portion of the total measured mass, the volume mean diameter changes more significantly (281 μm for the single-view results versus 239 μm from the crossed-beam configuration). Since the crossed-beam configuration removes many of the erroneous measurements, it is reasonable to expect this result to be of higher accuracy. Some further quantitative prove is given later in this work when data are compared with measurements from a higher magnification. Nevertheless, the detection and accurate measurement of spatially overlapped particles remains a challenge in DIH (Gao et al., 2014a; Wu et al., 2016).

Finally, and perhaps most important, the crossed-beam configuration is quite effective for measurement of out-of-plane particle velocities. For the interframe results, the change in z-positon given by the triangulation relation is

$$\Delta z = \Delta x_1 \cot(\theta) - \Delta x_2 \csc(\theta), \tag{4}$$

where Δx_1 and Δx_2 are the differences in measured x_1 and x_2 positions, respectively, during the interframe time, Δt. Importantly, Eq. (4), does not depend on any measured out-of-plane coordinates or on the translation constants, C_x, C_y, or C_z. The remaining calibration constant, θ, has relatively low uncertainty (see Table 1). Assuming the uncertainty in-plane coordinates (x_1 and x_2) is ~0.2 times the pixel size, the uncertainty in Δz is estimated to be 15 μm using the sum squared of component uncertainties (Kline and McClintock, 1953) and assuming average values of Δx_1 and Δx_2. This uncertainty is significantly less than the uncertainty in z-displacement measured by a typical single-view DIH configuration, and indicates that the crossed-beam, two-view configuration is particularly advantageous for measurement of out-of-plane displacements.

The bottom image in Fig. 6(b), shows the resulting out-of-plane, z-velocities measured at this condition. Compared to the single view results in Fig. 6(a), it is clear that the crossed-beam, two-view configuration significantly reduces the unrealistic scatter in the z-

velocities, and the results now qualitatively match intuition (main flow in the x-direction with some dispersion in the z-direction away from the center of breakup).

To better quantify these results, the conditions shown in Fig. 6 were repeated for 42 total realizations. Assuming negligible effects of gravity, process symmetry dictates that the observed scatter in the y-displacements will match that of the z-displacements. For all fragments measured in the view 1 configuration (Fig. 6(a) being one example realization), the standard deviation of the y-displacements is 22 μm while the standard deviation of z-displacements is 163 μm. The difference in these standard deviations gives an estimate of the uncertainty introduced by the depth-of-focus problem in single-view DIH (Katz and Sheng, 2010). For comparison with other results in the literature, this is normalized by the mean measured diameter at this condition ($D_{10} = 109$ μm) resulting in an estimated of depth-of-focus uncertainty of 1.3 mean particle diameters. In Gao et al. (2013a) detailed simulations and experiments are used to study the depth uncertainty of single-view DIH and the hybrid processing algorithms. In general, the depth measurement is found to be accurate to within 1 to 2 particle diameters, which is in good agreement with the current results.

With the crossed-beam configuration, the standard deviation of y-displacements is 20 μm, which closely agrees with the value measured from the single-view configuration in the previous paragraph. However, the standard deviation of z-displacements is reduced by an order of magnitude to 36 μm. Close agreement between the measured values in the y- and z-directions indicates that the crossed-beam configuration has largely eliminated the effects of the depth-of-focus problem on the out-of-plane velocities. It is unknown if the small remaining discrepancy is a result of physical effects of the flow or is caused by measurement uncertainties. Nevertheless, by analyzing the results in the same manner as the previous paragraph, it is found that the depth of focus uncertainty is reduced to 0.1 mean particle diameters or less.

2.5. High-magnification, single-view DIH configuration

The CCDs used here have a pixel size of 9 μm. In comparison, high-quality holographic plates can have spatial resolution as high as 5000 line-pairs/mm, enabling resolution of features as small as 0.2 μm. These differences significantly reduce the dynamic range of particle sizes which can be quantified with digital holography compared to analog holography. For example, here it is assumed particles must span at least three pixels for accurate quantification of size, and no region is accepted with $d < 27$ μm. In contrast, in previous investigations of drop breakup using analog holography fragments as small as 5 μm could be quantified (Hsiang and Faeth, 1992, 1993, 1995; Hwang et al., 1996; Chou et al., 1997; Chou and Faeth, 1998; Dai and Faeth, 2001).

To closely match this dynamic range, a high-magnification DIH configuration is used to investigate a few select conditions. This is constructed using a setup similar to the view 1 arrangement shown in Fig. 4 with the addition of a magnifying objective placed between the particle field and the CCD. Using techniques described in Gao et al. (2013b), calibration is performed to determine the effective pixel size of 2.4 μm, resulting in a minimum measurable diameter of 7.2 μm.

Each, high-magnification hologram is processed using methods similar to those described previously for the single-view DIH configuration, with the addition of a final depth refinement based on the sharpness profile method described in Gao et al. (2014a). This provides some improvement of the out-of-plane particle depth from single-view DIH, but at significantly increased computational costs.

3. Aerodynamic breakup results

The aerodynamic breakup of drops has been studied using the experimental methods described in the previous section. Here, results are presented for two air-flow rates, which correspond to conditions leading to breakup in the bag and sheet-thinning regimes (see Fig. 1). Table 2 summarizes the experimental conditions. In all cases, the syringe tip, shown in Fig. 3, is positioned at $y_0 = -174 \pm 5$ mm above the center line of the air-nozzle. The initial drop diameter, d_0, and the x-location where the drop is injected into the air flow, x_0, are measured from 20 holograms of the drop falling with the air jet turned off, and uncertainty reported in Table 2 is the standard deviation of these measured quantities. The initial centerline air velocity, u_0, is estimated from previous measurements of this flow (Guildenbecher, 2009; Flock et al., 2012), with the root mean square of the flow fluctuations used to estimate uncertainty (Guildenbecher, 2009). Before entering the air jet, the initial drop velocity can be assumed to be zero in the x- and z-direction, and the initial droplet y-velocity, v_{y0}, is well approximated by

$$v_{y0} = \sqrt{2g(y - y_0)}, \tag{5}$$

where g is the acceleration due to gravity. For example, with the air-nozzle turned off, the measured v_{y0} at $y = 0$ is 1.8 ± 0.2 m/s, while the value estimated by Eq. (5) is 1.8 m/s. Finally, *We*, shown in Table 2, is found from Eq. (1), with uncertainty estimated by standard propagation techniques (Kline and McClintock, 1953).

For consistency with previous work (Flock et al., 2012; Gao et al., 2013b; Gao et al., 2014b; Gao et al., 2015), in the calculation of *We* in Table 2, we have chosen to determine the initial relative velocity, u_0, using the estimated centerline air velocity, neglecting the small contribution due to the initial drop velocity, v_{y0}. Inclusion of v_{y0} has a minor effect on the measured *We* and does not affect the predicted breakup morphology. More importantly, for those interested in utilizing the data reported here for the purposes of model validation, we recommend careful consideration of the effects of the spatially varying air velocity, caused by expansion of the free air jet. Unlike experiments in a shock tube, which produce a nearly ideal, step-change in gas-velocity (Hsiang and Faeth, 1992, 1993, 1995; Chou et al., 1997; Chou and Faeth, 1998; Dai and Faeth, 2001; Theofanous, 2011), the continuous air jet utilized here imposes a spatially varying gas velocity along the trajectory of the deforming and fragmenting drop. While this adds some complexity for modeling, the advantage of the current experimental configuration is the ability to inject a steam of droplets such that conditions can be repeated quickly for quantification of statistics.

3.1. Breakup in the bag regime

The temporal history of the breakup process is investigated at the conditions in the first row of Table 2. By translating the air-nozzle and droplet generator with respect to the DIH fields of view and adjusting the recording delay with respect to the triggering of the HeNe laser shown in Fig. 3, 16 different locations along the trajectory of the deforming and fragmenting drop are investigated. At each location, approximately 44 realizations of drop breakup are recorded using the two-view, crossed-beam DIH methodology discussed in the previous section. On average approximately 10,000 fragments are measured at each location.

Fig. 7 summarizes the experimental results. Here, select results are shown at six of the positions investigated. At each location, the top row shows a sample view 1 hologram image, which has been numerically refocused to the approximate center of the breakup event. Overlaid are the in-plane fragment sizes and velocities, measured with the crossed-beam, two-view DIH methodology described in the previous section. The second and third row, show

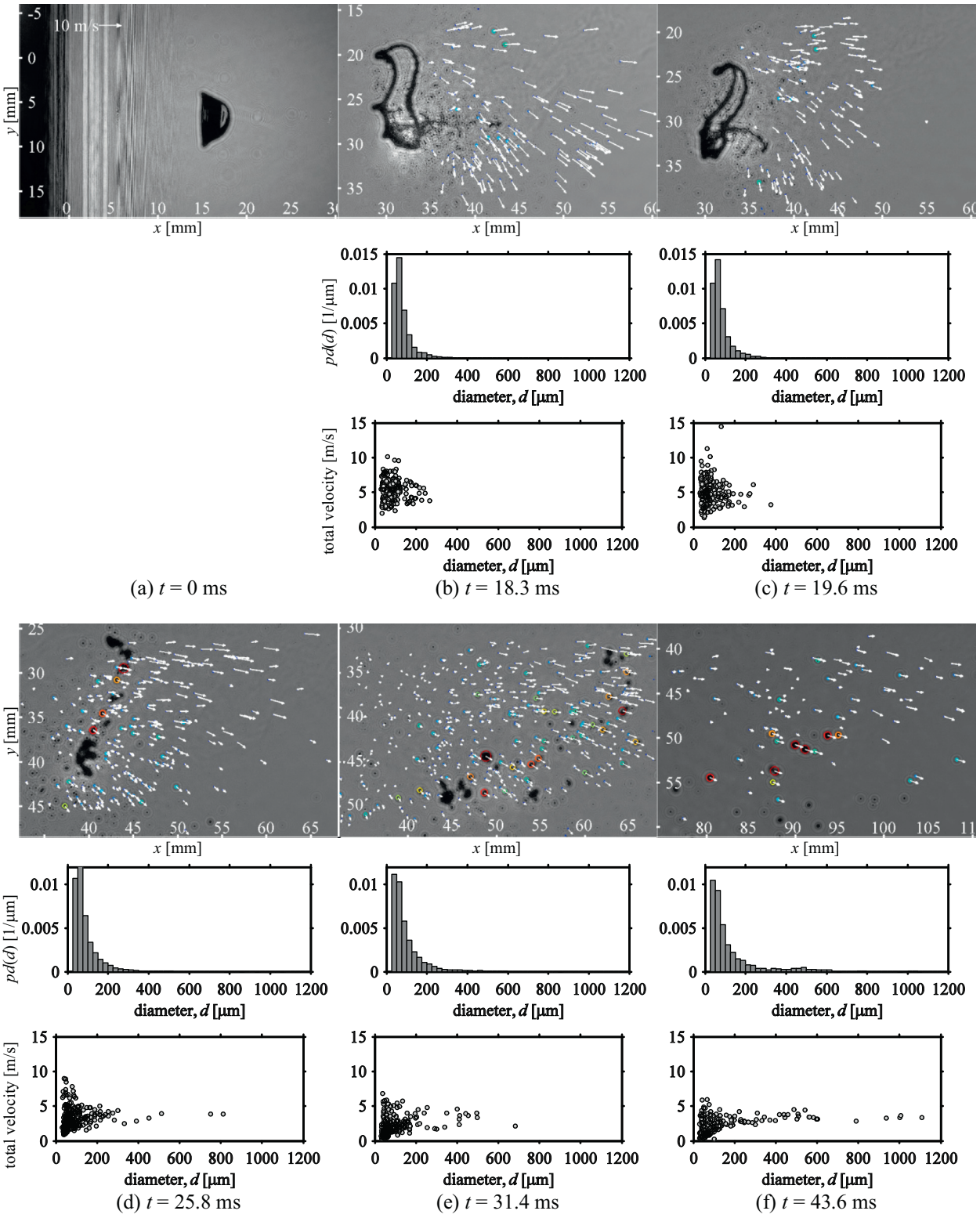

Fig. 7. Selected DIH results for $We = 13.8 \pm 0.5$. All images are of the view 1 hologram refocused to the mean z-location, then overlaid with the in-plane velocities and sizes measured from the dual-view configuration (see Fig. 6 for size color scale; all times are relative to that of the first image). The number probability density, $pd(d)$, is measured from approximately 44 realizations at each condition. Finally, size-velocity maps are built from all realizations (250 data points shown, selected at random from all measured fragments).

Table 2
Initial conditions for the two secondary breakup morphologies.

Morphology	Initial drop x-location, x_0 [mm]	Initial drop diameter, d_0 [mm]	Air mass flow-rate [kg/min]	Centerline air velocity at x_0, v_0 [m/s]	Centerline turbulence intensity at x_0	Air-jet Reynolds number	Drop Weber number, *We*
Bag	8.8 ± 0.1	2.54 ± 0.02	0.35	10.5 ± 0.2	1.9%	1.8×10^4	13.8 ± 0.5
Sheet-thinning	8.9 ± 0.2	2.55 ± 0.01	0.70	21.0 ± 0.5	2.4%	3.5×10^4	55.3 ± 2.6

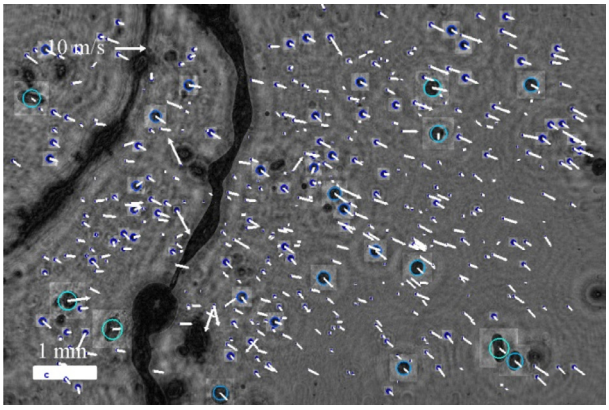

Fig. 8. Example high-magnification DIH result at $We = 13.8 \pm 0.5$, $t = 18.3$ ms. Background shows the recorded hologram refocused to a plane containing the intact ring structure. Bright squares show the particle image refocused to their measured z-locations. (See Fig. 6 for size color scale).

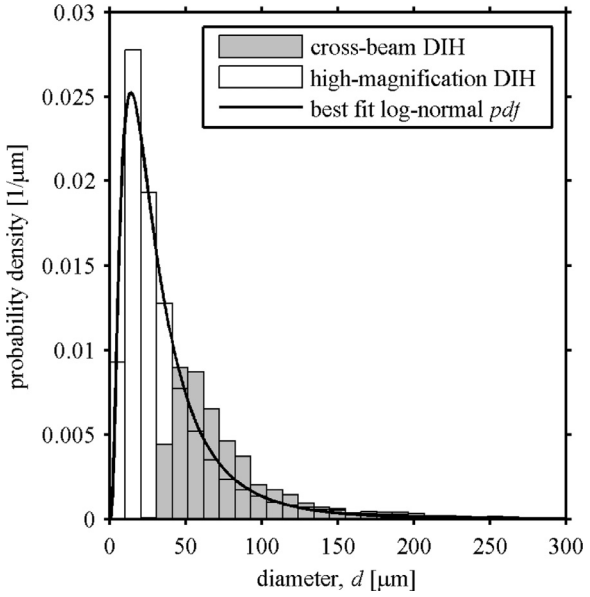

Fig. 9. Size probability density measured with the crossed-beam DIH configuration and a single-view high-magnification DIH configuration at $We = 13.8 \pm 0.5$, $t = 18.3$ ms. Here the crossed-beam probability density is scaled by the percent of fragments measured in the high-magnification results with $d > 27$ μm. The solid line is the best-fit log-normal *pdf* corresponding to the high-magnification results.

the measured probability density of fragment sizes and a scatter plot of sizes vs total velocities, respectively. These are determined using all fragments measured from all 44 realizations of the flow. Finally, the captions show the time delay of the recording with respect to the first image, while the x-y coordinates of the field of view are shown overlaid on the image in the top row. (Note, Fig. 7(e) corresponds to the conditions presented in detail in the previous section.)

Results in Fig. 7 illustrate the classical bag-breakup morphology, which begins with the formation of a thin bag-like structure attached to a thick toroidal rim. Breakup of the bag occurs at $t \approx 20$ ms, resulting in a number of small fragments with $d \lesssim 200$ μm. The total velocity of the fragments produced by breakup of the bag displays a large amount of scatter. This is particularly true for the smallest measured fragments, which display $\pm \sim 2.5$ m/s variations in total velocity. These variations are significantly higher than the measured gas-phase turbulence fluctuations in the absence of the drop (~ 0.2 m/s) (Guildenbecher, 2009), indicating that fragment velocity fluctuations are a result of the bag breakup process, possibly including the effects of increased gas-phase turbulence in the drop's wake (Flock et al., 2012). Finally, rim fragmentation occurs at $t \gtrsim 20$ms, resulting in the production of a few large fragments with $d \gtrsim 200$ μm. These rim fragments tend to display much less velocity fluctuations compared to the bag fragments.

Careful investigation of the images in Fig. 7 indicates that the crossed-beam DIH configuration does not detect all of the smallest fragments in the flow. This is likely because many fragments are smaller than the minimum size detection limit of 27 μm. To better quantify these small particles, the high-magnification DIH configuration is used to record 175 image pairs at approximately $t \approx 19$ ms, corresponding to the conditions illustrated in Fig. 7(b) and (c). At this time, breakup of the bag is essentially complete, while the rim remains intact. Fig. 8 shows one example result. Quantitative comparison of the number density of fragments measured in this high-magnification result with Fig. 7(b) and (c) clearly indicate that

Table 3
Comparison of characteristic mean diameters measured at $We = 13.8 \pm 0.5$, $t = 18.3$ ms using the crossed-beam DIH configuration and a single-view high-magnification DIH configuration.

DIH configuration	D_{10} [μm]	D_{30} [μm]	D_{32} [μm]	MMD [μm]
Crossed-beam	79 ± 8	118 ± 26	185 ± 89	242 ± 145
High-magnification	39 ± 8	80 ± 18	158 ± 42	223 ± 63

the high-magnification DIH configuration is able to quantify many small particles, which are below the size detection limit of the crossed-beam DIH configuration.

These differences are quantified by the comparison of measured fragment size probability densities in Fig. 9. Clear bars show the size probability density measured with the high-magnification DIH configuration. These results appear to be well described using a log-normal probability density function as shown by the solid black line. Finally, gray bars show the size probability density measured with the crossed-beam DIH configuration. To account for the percent of fragments below the size detection limit of the crossed-beam DIH configuration, the gray bars are scaled such that their integral is equal to the percent of fragments with $d > 27$ μm as quantified by the high-magnification results.

Although the comparison is not perfect, the general agreement between the size probability densities at $d > 27$ μm increases our confidence that both configurations accurately quantify the fragments in this size range. In addition, these results clearly demonstrate the limited size dynamic range of the crossed-beam DIH configuration. Those interested in using these data for model validation should carefully account for these effects. Finally, Table 3

summarizes the characteristic mean diameters quantified from both configurations. Here, characteristic mean diameters are defined as

$$D_{pq} = \left[\sum d^p / \sum d^q\right]^{1/(p-q)}, \quad (6)$$

where p and q are defined by the subscripts shown in Table 3. MMD is the mass median diameter defined as the diameter for which half of the measured mass is contained in particles of smaller diameter. As would be expected, the results in Table 3 show that the characteristic mean diameters measured with the crossed-beam DIH configuration are always greater than the high-magnification results. This is most dramatic for the number mean diameter, D_{10}. Higher order mean diameters, which tend to more heavily weight fragments of larger diameter, show better agreement between the two magnification levels. Importantly, the Sauter mean diameter, D_{32}, and MMD agree to within 17% and 9% respectively. This provides an estimate of an appropriate confidence interval when these values are used for comparison with previous literature later in this discussion.

Prior to this investigation, the only other work which has attempted to investigate the temporal dynamics of bag breakup may be that of Chou and Faeth (1998). There, analog holography was used to quantify fragment properties from the breakup of a drop in a shock-tube. Despite the aforementioned differences in the gas-phase boundary conditions, many of the conclusions from Chou and Faeth (1998) are in good agreement with the current results. In particular, the breakup process is observed to occur over an extended time and spatial domain, indicating that models which treat breakup as instantaneous (O'Rourke and Amsden, 1987; Reitz, 1987) have inherent limitations. Furthermore, Chou and Faeth (1998) conclude that rim breakup results in fragments with mean sizes approximately $0.3{\cdot}d_0$. This corresponds to ~750 μm for the d_0 investigated here. While the current work lacks sufficient temporal results to definitively identify the fragments produced from the rim versus those from the bag, in Fig. 7 it is clear that the largest drops, which almost certainly originate from breakup of the rim, have a mean size close to this value. Finally, in agreement with current observations, Chou and Faeth (1998) conclude that the rim fragment velocities are independent of size.

On the other hand, a number of significant differences are observed when comparing the properties of the fragments from the early-time breakup of the bag. For example, Chou and Faeth (1998) conclude that breakup of the bag results in a nearly monodisperse fragment size distribution with approximately constant velocities equal to the velocity of the initial drop. In contrast, Fig. 7 results indicate that bag breakup leads to a polydisperse fragment size distribution with significant velocity fluctuations. The exact cause of these differences with the Chou and Faeth (1998) work is not clear. Perhaps the gas-phase turbulence is higher in the expanding free-jet investigated here compared to the confined shock-tube flow investigated in Chou and Faeth (1998). Due to their small size, higher gas-phase turbulence would more strongly affect the bag fragments compared to the rim fragments, which may explain the higher bag fragment velocity variations observed here. In addition, at the time of Chou and Faeth's (1998) investigation, holograms were manually post-processed to locate particles, as a consequence they report measuring only 100 to 200 fragments per condition, whereas here over 10,000 fragments are measured per location. It is possible that Chou and Faeth (1998) measured an insufficient number of fragments to quantify the statistical details observed here.

The distinct bag and rim features, along with potentially different instability mechanisms controlling the breakup of these features, have led a number of authors to speculate that these conditions would lead to a multi-modal fragment size distribution

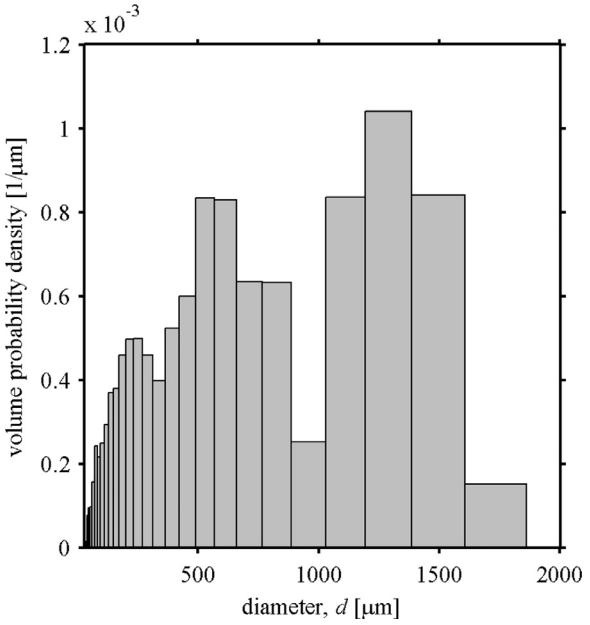

Fig. 10. Volume probability density for all fragments measured at $We = 13.8 \pm 0.5$, $t = 31.4$ ms, which corresponds to the conditions shown in Fig. 7(e). Note the multi-modal distribution with a peak at ~250 μm likely due to bag fragments, a peak at ~550 μm likely due fragments from the cylindrical portion of the rim, and ~1300 μm likely due to rim node fragments.

(Guildenbecher et al., 2009). However, previous experimental evidence is mixed with some reporting a multi-modal distribution (Komabayasi et al., 1964) while others report data that is well described by a distribution with a single mode (Chou and Faeth, 1998). The cause of this disagreement may be understood by careful inspection of the results in Fig. 7. There, measured fragment sizes are plotted as a probability density weighted by count. Due to the small number of rim fragments compared to bag fragments, the probability densities appear nearly mono-modal. In contrast, Fig. 10 replots the data in Fig. 7(e) ($We = 13.8 \pm 0.5$, $t = 31.4$ ms) as a probability density weighted by volume. This is found by multiplying the number probability density by the cube of the diameter and represents the probability that the total volume is made up of fragments of diameter, d. Replotted in this way, Fig. 10 shows a clear multi-modal distribution with three distinct peaks at ~250, 550, and 1300 μm. From this it can be concluded that the fragment size distribution is indeed multi-modal, and previous investigators, which reported a single-model distribution, likely only considered the probability density by count.

The observed peak at the smallest diameter is almost certainly due to bag fragments, while the remaining larger fragments likely originate from the rim. Assuming all fragments with $d > 350$ μm originate from the rim, results in an estimated volume fraction of rim fragments of 88%. In Gao et al. (2013b), digital holograms were used to directly measure the shape and volume of the rim, with Fig. 2(b) showing an example result. From that analysis, the volume fraction of the rim was found to be about 90%. Because both the current results and the Gao et al. (2013b) measurement were performed in the same experimental facility with nominally the same conditions while using two alternative techniques that result in nearly identical volume fraction measurements, the confidence in this quantity for the current conditions is rather high. In contrast, Chou and Faeth (1998) explored a broader range of conditions and reported an average rim volume fraction of 56% while early work by Lane (1951) estimated the rim volume fraction around 75%. Although the accuracy of the Lane (1951) and

Chou and Faeth (1998) data is less well understood, these various results indicate that volume fraction of the rim may not be constant and instead likely is a function of operating conditions and experimental configuration. More work would be needed to quantify these effects.

As noted by Chou and Faeth (1998) breakup of the rim produces fragments of two size classes. Most of the rim begins as a roughly cylindrical structure which breaks due to the capillary instability forming fragments of moderate size. In addition, a few large nodes also tend to form on the rim at early times. For example, Fig. 7(b) clearly shows a few, large backward facing protrusions along the intact rim. These so called "nodes" tend to persist for some time and eventually result in a few large node fragments. These observations indicate that the intermediate peak at ~550 μm in Fig. 10 is likely due the fragments from the cylindrical portion of the rim, while the peak at ~1300 μm is likely from node drops.

3.2. Breakup in the sheet-thinning regime

The experiments and data processing methods are repeated for a higher air velocity corresponding to the conditions given in the second row in Table 2. Twelve different locations along the trajectory of the deforming and fragmenting drop are investigated. At each location, approximately 44 realizations of drop breakup are recorded. Fig. 11 summarizes the measured results. At this higher *We*, the bag like structure is no longer observed, rather fragments break off from thin sheets which form at the periphery of the deformed droplet. Based on such observations, this breakup mechanism is referred to as the sheet-thinning morphology (sometimes alternatively referred to as shear-induced breakup).

Results in Fig. 11 show the classical sheet-thinning breakup morphology. At early times, e.g. Fig. 11(a), the high gas-velocity at the periphery of the deformed drop results in the formation of thin sheet-like membranes. As time progresses, these sheets are stretched downstream where they fragment. From the images in the top row in Fig. 11 it is clear that this breakup mechanism continues for some time until most, if not all, of the original intact core drop has been stripped away into secondary fragments. With increasing time the fragment size probability densities in the second row of Fig. 11 tend to show comparatively more fragments at larger diameters. This is likely due to the continuous acceleration of the intact core by aerodynamic drag which reduces the gas-liquid relative velocity and, therefore, the disruptive aerodynamic forces. Finally, compared to the bag breakup case, the size-velocity plots in the third row in Fig. 11 show a much more obvious size-velocity correlation with the smallest fragments traveling fastest due to aerodynamic drag.

Unlike the bag breakup case, most authors agree that fragments produced by the sheet-thinning mechanism display a mono-modal size-distribution (Guildenbecher et al., 2009). This seems to be confirmed by the probability densities by count shown in Fig. 11, which all appear to have a single, distinct peak. This is further verified by Fig. 12, which replots the data in Fig. 11(e) ($We = 55.3 \pm 2.6$, $t = 26.8$ ms) as a probability density weighted by volume. Again, unlike the bag breakup case in Fig. 10, this volume probability density clearly contains only one distinct peak. This all tends to confirm the assumption that the sheet-thinning morphology produces fragments by one instability mechanism. In addition, the data is fit to a root-normal *pdf* as suggested by Simmons (1977) and Chou et al. (1997). This is discussed further in the subsequent section on ensemble results.

Once again, the only other work, which investigated the temporal dynamics of sheet-thinning breakup, may be that of Chou et al. (1997) who utilized the same shock-tube experimental configuration and analog holography diagnostics of Chou and Feath (1998) discussed in the previous section. Similar to the bag breakup case, many observations of Chou et al. (1997) agree with the results in Fig. 11. Specifically, sheet-thinning breakup is observed to be a continuous process which occurs over relatively long temporal and spatial scales. In addition, at early times Chou et al. (1997) concluded that the mean fragment sizes tend to increase with respect to time, while at late times a quasi-steady behavior is observed wherein all new fragments produced tend to have a roughly constant mean diameter. However, if the total breakup time is relatively short only the initial transient fragment size behavior is observed, and Chou et al. (1997) conclude that the transition between fully transient fragment size behavior and breakup which includes some quasi-steady behavior occurs at a liquid phase Reynolds number, Re_l, of ~2750 where momentum scaling is used to derive a characteristic liquid phase velocity resulting in $Re_l = (\rho_g \rho_l)^{1/2} u_0 d_0 \mu_l^{-1}$. For the conditions investigated here $Re_l = 1370$ which is less than the transition Re_l such that Chou et al. (1997) predict only the transient fragment size behavior. Indeed, results in Fig. 11 appear to indicate that larger drops are produced at later times and, therefore, mean fragment diameters are likely to be continuously increasing. These observations are further quantified in the next section.

Finally, some differences with the Chou et al. (1997) results are also noted. Once again, the limitations of the analog holography configuration employed by Chou et al. (1997) restricted the total number of fragments, which could be quantified at each conditions. Perhaps as a result of this, Chou et al. (1997) observed no clear relation between fragment sizes and velocities. In contrast the current results show a clear size-velocity correlation, which is generally expected due to aerodynamic drag. Here, digital holography has enabled many orders of magnitude increase in the number of measurements at each condition. Consequently, it appears that the current experiment has resolved some detailed trends which were not previously observed.

3.3. Ensemble fragment statistics

To further quantify temporal effects, Fig. 13 summarizes the characteristic mean diameters as defined by Eq. (6). In this figure, each data point is found from the ensemble of all 44 realizations at the *We* and delay times shown. Uncertainty bars are the standard deviation in these quantities from each realization. The mean fragment sizes tend to increase with respect to time. This is likely due to the reduced relative velocity between the core drop and gas phase as time progresses, which results in reduced aerodynamic energy to drive fragmentation. Interestingly, at early times the higher *We* case appears to produce larger fragments. This may be because the sheet-thinning mechanism produces larger fragments compared to those resulting from rupture of the thin bag. In contrast, the lower *We* case displays larger characteristic mean diameters at later times, particularly with respect to D_{32} and MMD which tend to be most heavily weighted by the largest fragments. This observation is likely due to rim collapse, which produces a few very large fragments at late times in the bag breakup case.

The Satuer mean diameter, D_{32}, is often believed to be the most important characteristic diameter because of its relation to the mean surface area to volume ratio of importance to many combustion phenomena. For this reason, a number of previous authors have focused on quantifying D_{32} of fragments due to aerodynamic breakup of drops. For example, the two open symbols on the right hand side of Fig. 13(b) are from the semi-empirical correlation of fragment sizes after completion of breakup provided Hsiang and Faeth (1992) (Eq. (14) in that work). The open circle represents D_{32} predicted by the Hsiang and Faeth (1992) results for the $We = 14$ condition investigated here, while the open triangle corresponds to the $We = 55$ condition. As shown in Figs. 7 and 11, at the latest times investigated here, the breakup process is essentially com-

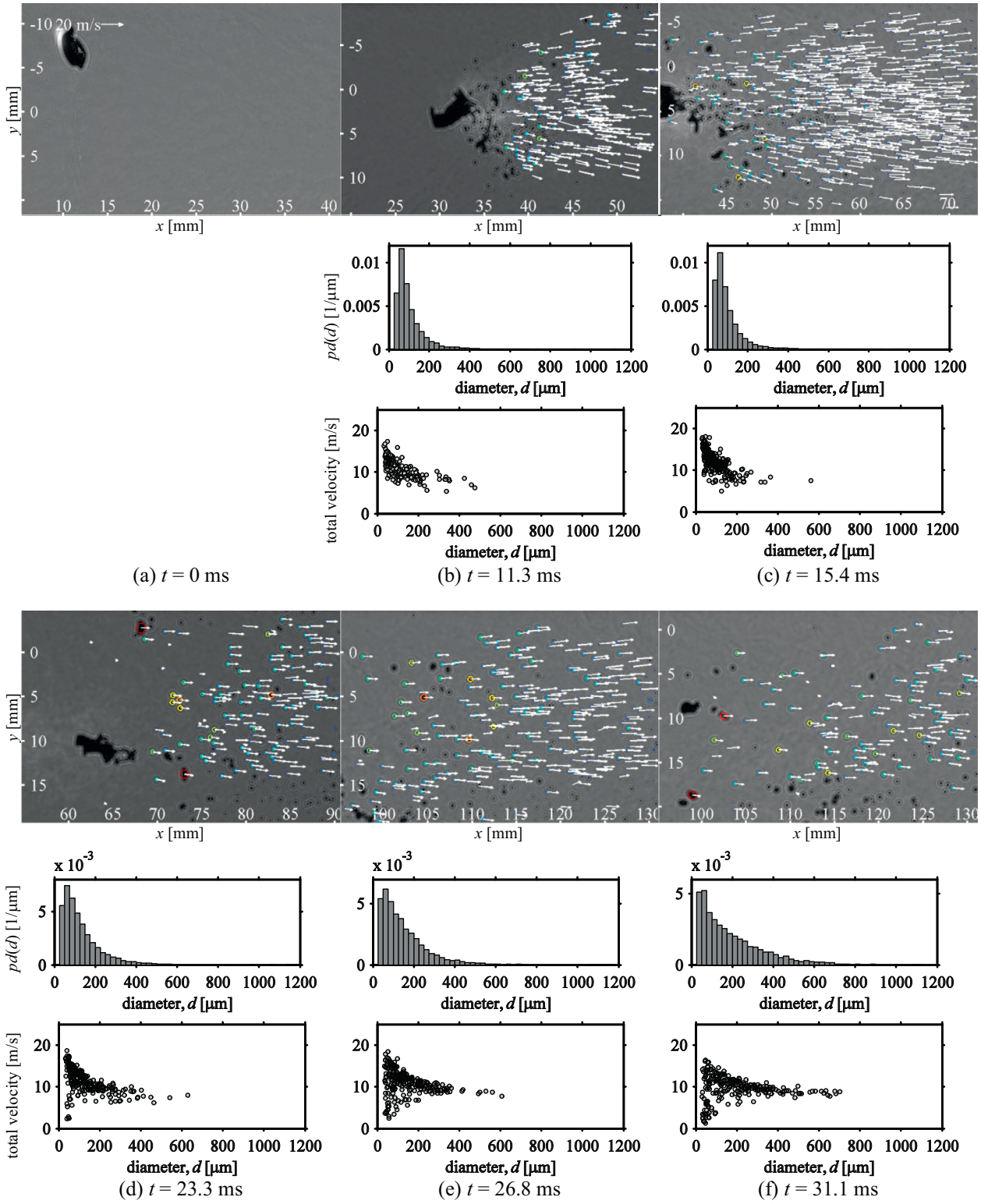

Fig. 11. Selected DIH results for $We = 55.3 \pm 2.6$. All images are of the view 1 hologram refocused to the mean z-location, then overlaid with the in-plane velocities and sizes measured from the dual-view configuration (see Fig. 6 for size color scale; all times are relative to that of the first image). The number probability density, $pd(d)$, is calculated from 44 realizations at each condition. Finally, size-velocity maps are built from all realizations (250 data points shown, selected at random from all measured fragments).

plete, and indeed D_{32} measured at the final times reported here ($t = 43.6$ ms for $We = 14$, and $t = 31.1$ ms for $We = 55$) appears to reasonably match the semi-empirical results of Hsiang and Faeth (1992). This is further quantified by Table 4 which summarizes the characteristic mean diameters at the final times measured here. Predicted values of D_{32} from the Hsiang and Faeth (1992) correlation are 603 and 426 μm for $We = 14$ and 55, respectively. These quantities agree to within 20% of the measured values given in Table 4. Given the measurement scatter and the possible biases in the measured quantities due to the minimum measurable fragment

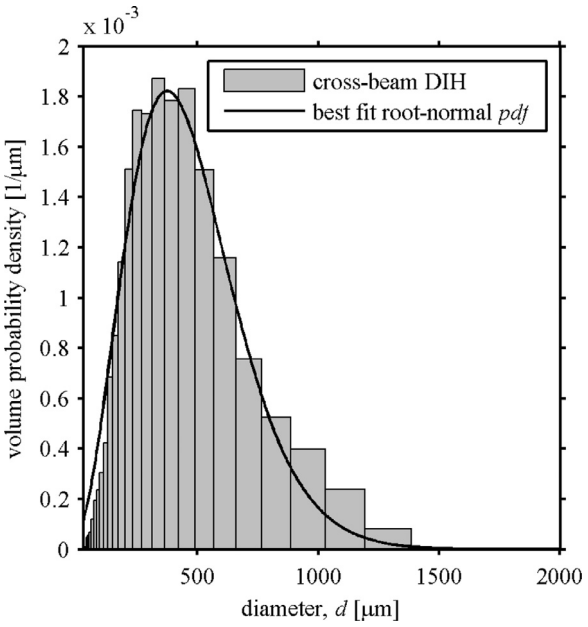

Fig. 12. Volume probability density for all fragments measured at $We = 55.3 \pm 2.6$, $t = 26.8$ ms, which corresponds to the conditions shown in Fig. 11(e). Note the distribution appears mono-modal with one peak at approximately 350 μm. The solid line is the best-fit root-normal *pdf*.

diameter as discussed in the previous section, this level of agreement seems reasonable.

Similar to the current work, Chou et al. (1997) also provides some quantification of D_{32} with respect to time. For example, the line shown in Fig. 13(c) shows the temporal scaling of, D_{32}, predicted by the semi-empirical theory presented in Chou et al. (1997) for the sheet-thinning case (Eq. (7) in that work). At intermediate times this theory matches reasonably well with the current measurements at $We = 55$. However, at early and late times, agreement is less than satisfactory. This hints that the simple model in Chou et al. (1997) may not full capture all details of the fragmentation physics. For example, the Chou et al. (1997) theory is based upon the assumption that fragments are stripped from the boundary layer at the periphery of the deformed drop. This assumption has been debated in the literature, with others proposing alternative mechanisms (Liu and Reitz, 1997; Theofanous, 2011). Due to the scatter in the current results (as well as the Chou et al., 1997 measurements) it is currently unclear if the observed similarities with the theory are reflective of the breakup physics or are a more coincidental effect of an empirical constant used in the Chou et al. (1997) derivation.

Table 4
Characteristic mean diameters after completion of breakup for the two conditions investigated.

Weber number, *We*	D_{10} [μm]	D_{30} [μm]	D_{32} [μm]	MMD [μm]
13.8 ± 0.5	138 ± 33	299 ± 71	583 ± 140	736 ± 160
55.3 ± 2.6	200 ± 31	327 ± 53	509 ± 117	602 ± 139

Early atomization investigations by Simmons (1977) suggested that many spray processes result in volumetric fragment size distributions which are well described by the universal root-normal *pdf* with $MMD/D_{32} \approx 1.2$. When true, this suggests that knowledge of D_{32} alone is sufficient to fully determine the fragment size distribution. Further work by Hsiang and Faeth (1992), Chou et al. (1997) and Chou and Faeth (1998) suggested that the breakup of an isolated drop in a cross-flow can also result in a distribution with $MMD/D_{32} \approx 1.2$. To investigate this possibility for the current data, Fig. 14 plots the ratio of MMD/D_{32} for the experimental times investigated here. Similar to the results of Chou and Faeth (1998), for the bag breakup case ($We = 14$) this ratio is closer to 1.0 at early times and then significantly exceeds 1.2 at late times. In addition, as already noted in Fig. 10, the volume distribution from bag breakup is clearly multimodal. Together, these results suggest that the mono-modal universal root-normal distribution is not appropriate for the bag breakup case. On the other hand, in agreement with the results of Chou et al. (1997), the ratio of MMD/D_{32} for the sheet-thinning case ($We = 55$) is much closer to 1.2 for all mea-

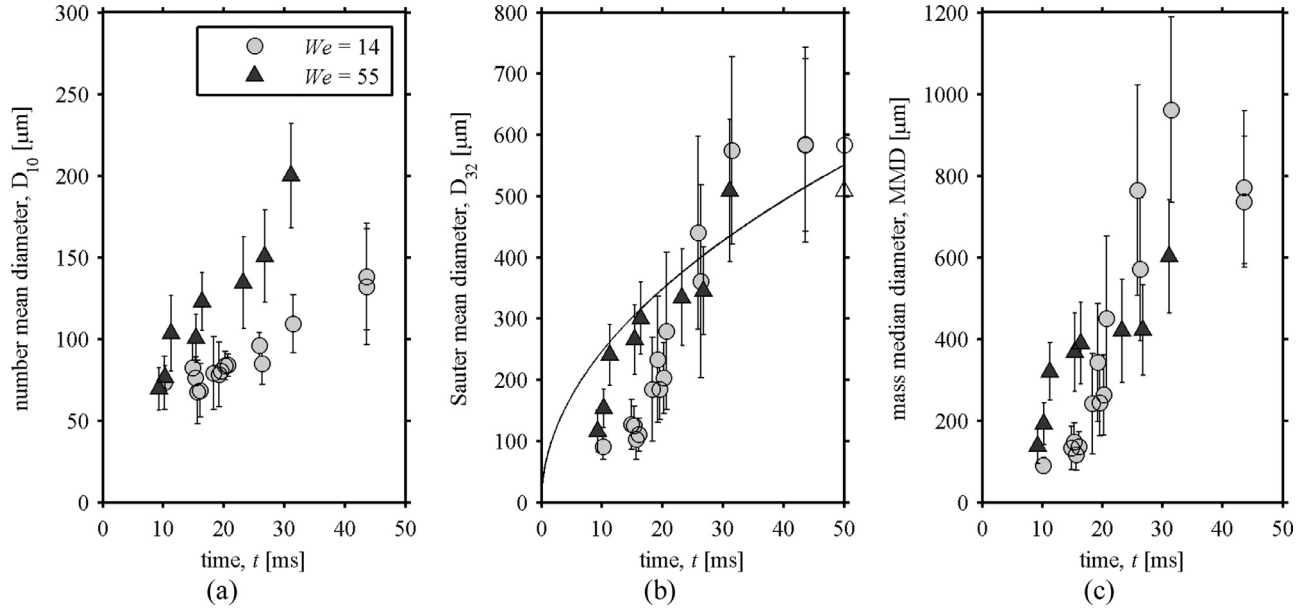

Fig. 13. Evolution of characteristic mean drop sizes: (a) number mean diameter, D_{10}, (b) Sauter mean diameter, D_{32}, and (c) mass median diameter, MMD. Symbols show the mean from all results and uncertainty bars are the standard deviation of the measured quantity from each of the 44 realizations. In (b) open symbols show the predicted final D_{32} based on the semi-empirical relationship of Hsiang and Faeth (1992) while the solid line shows the temporal scaling predicted by Chou et al. (1997) for the sheet-thinning case.

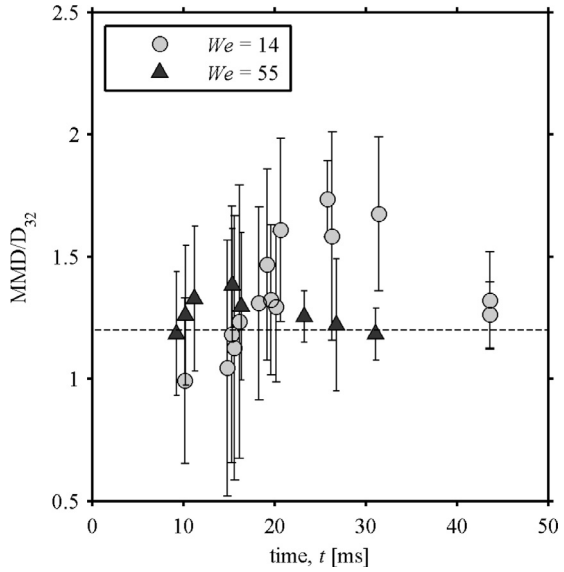

Fig. 14. Ratio of mass median diameter, MMD to Sauter mean diameter, D_{32}, versus time. Dotted line shows $MMD/D_{32} = 1.2$ corresponding to the universal root-normal distribution proposed by Simmons (1977).

sured times. In addition, as noted in Fig. 12 the volume distribution is mono-modal and can be well described by the root-normal distribution. These results suggest that the universal root-normal distribution may provide a reasonable approximation of the results for breakup at higher *We*.

4. Summary and conclusions

The fragmentation of ethanol drops in a continuous air stream is experimentally investigated. Digital in-line holography (DIH) is introduced for quantification of fragment sizes, three-dimensional positions, and three-component velocities within a large measurement volume. To address the depth of focus problem commonly encountered in DIH, a crossed-beam, two-view configuration is proposed. Here, a narrow stereo angle in employed between the two DIH fields of view. Compared to previous two camera DIH configurations, which utilize orthogonal fields of view, the current configuration enables a larger overlapping measurement volume and can be utilized in facilities with limited optical access. By leveraging expected flow symmetries in the particle field investigated here, the crossed-beam, two-view DIH configuration is shown to reduce uncertainty of measured fragment velocities in the depth direction by at least an order of magnitude compared to traditional single camera DIH.

This experimental configuration is employed to investigate the fragmentation of ~2.5 mm ethanol drops injected into an air jet with core flow velocities of 10.5 and 21.5 m/s. These conditions correspond to non-dimensional Weber numbers, *We*, of ~14 and 55. At the lower *We* the classical bag breakup morphology is observed with the formation of a thin bag-like structure attached to a thick toroidal rim. Breakup begins with shattering of the bag followed by fragmentation of the rim at late times. To study the temporal fragment statistics during the course of breakup, multiple experiments are performed in which individual drops are recorded at different delay times with respect to the start of the deformation process. Ensemble averaging reveals that fragment are initially small due to shattering of the thin bag. At late time, rim fragmentations results in a few large fragments. The resulting fragment size distribution is shown to be multi-modal due to the varied instability mechanisms controlling the breakup of the bag and rim structures.

At the higher *We* the sheet-thinning breakup morphology is observed. At this condition, fragments are continuously stripped from sheet-like structures which form at the periphery of the deformed core drop. As time progresses, ensemble averaging shows that mean fragment sizes continuously increase. The resulting volumetric fragment size distribution is shown to contain a single peak which is well described by the universal root-normal distribution proposed by Simmons (1977).

In the results reported here, approximately 10,000 fragments are measured per condition. Compared to previous investigations which quantified only a few hundred fragments per condition (Chou et al., 1997; Chou and Faeth, 1998), the current work significantly reduces the uncertainty in measured fragment statistics and reveals detailed trends which were not previously observed. Combined with earlier experimental work focused on the initial deformation of the drops (Flock et al., 2012), the current experimental dataset is expected to provide new opportunities for detailed model development and validation.

Acknowledgements

This work was supported by the Laboratory Directed Research and Development program at Sandia National Laboratories which is a multiprogram laboratory operated by Sandia Corporation, a Lockheed Martin Company, for the U.S. Department of Energy's National Nuclear Security Administration under contract no. DE-AC04-94AL85000.

References

Arienti, M., Li, X., Soteriou, M.C., Eckett, C.A., Sussman, M., Jensen, R.J., 2013. Coupled level-set/volume-of-fluid method for simulation of injector atomization. J. Propul. Power 29, 147–157.
Arienti, M., Pan, W., Li, X., Karniadakis, G., 2011. Many-body dissipative particle dynamics simulation of liquid/vapor and liquid/solid interactions. J. Chem. Phys. 134, 204114.
Buchmann, N.A., Atkinson, C., Soria, J., 2013. Ultra-high-speed tomographic digital holographic velocimetry in supersonic particle-laden jet flows. Meas. Sci. Technol. 24, 024005.
Chou, W.H., Faeth, G.M., 1998. Temporal properties of secondary drop breakup in the bag breakup regime. Int. J. Multiphase Flow 24, 889–912.
Chou, W.H., Hsiang, L.P., Faeth, G.M., 1997. Temporal properties of drop breakup in the shear breakup regime. Int. J. Multiphase Flow 23, 651–669.
Dai, Z., Faeth, G.M., 2001. Temporal properties of secondary drop breakup in the multimode breakup regime. Int. J. Multiphase Flow 27, 217–236.
Desjardins, O., Moureau, V., Pitsch, H., 2008. An accurate conservative level set/ghost fluid method for simulating turbulent atomization. J. Comput. Phys. 227, 8395–8416.
Flock, A.K., Guildenbecher, D.R., Chen, J., Sojka, P.E., Bauer, H.J., 2012. Experimental statistics of droplet trajectory and air flow during aerodynamic fragmentation of liquid drops. Int. J. Multiphase Flow 47, 37–49.
Gao, J., Guildenbecher, D.R., Engvall, L., Reu, P.L., Chen, J., 2014a. Refinement of particle detection by the hybrid method in digital in-line holography. Appl. Opt. 53, G130–G138.
Gao, J., Guildenbecher, D.R., Hoffmeister, K.N.G., Chen, J., Sojka, P.E., 2015. Characterization of drop aerodynamic fragmentation in the bag and shear thinning regimes by crossed-beam two-view digital in-line holography. ILASS Americas 27th Annual Conference on Liquid Atomization and Spray Systems. Raleigh, North Carolina.
Gao, J., Guildenbecher, D.R., Reu, P.L., Chen, J., 2013a. Uncertainty characterization of particle depth measurement using digital in-line holography and the hybrid method. Opt. Express 21, 26432–26449.
Gao, J., Guildenbecher, D.R., Reu, P.L., Chen, J., 2014b. Characterization of aerodynamic fragmentation of a drop by cross-beam two-view digital in-line holography. ILASS Americas 26th Annual Conference on Liquid Atomization and Spray Systems. ILASS, Portland, OR.
Gao, J., Guildenbecher, D.R., Reu, P.L., Kulkarni, V., Sojka, P.E., Chen, J., 2013b. Quantitative, 3D diagnostics of multiphase drop fragmentation via digital in-line holography. Opt. Lett. 38, 1893–1895.
Gorokhovski, M., Herrmann, M., 2008. Modeling primary atomization. Annu. Rev. Fluid Mech. 40, 343–366.
Guildenbecher, D., López-Rivera, C., Sojka, P., 2009. Secondary atomization. Exp. Fluids 46, 371–402.
Guildenbecher, D.R., 2009. Secondary Atomization of Electrostatically Charged Drops. Mech. Eng. Purdue University, West Lafayette, Indiana.
Guildenbecher, D.R., Gao, J., Reu, P.L., Chen, J., 2013. Digital holography simulations and experiments to quantify the accuracy of 3D particle location and 2D sizing using a proposed hybrid method. Appl. Opt. 52, 3790–3801.

Guildenbecher, D.R., Sojka, P.E., 2011. Experimental investigation of aerodynamic fragmentation of liquid drops modified by electrostatic surface charge. Atomization Sprays 21, 139–147.
Han, J., Tryggvason, G., 1999. Secondary breakup of axisymmetric liquid drops. I. Acceleration by a constant body force. Phys. Fluids 11, 3650–3667.
Han, J., Tryggvason, G., 2001. Secondary breakup of axisymmetric liquid drops. II. Impulsive acceleration. Phys. Fluids 13, 1554–1565.
Herrmann, M., 2010. Detailed numerical simulations of the primary atomization of a turbulent liquid jet in crossflow. J. Eng. Gas. Turb. Power 132 061506-061506.
Hsiang, L.P., Faeth, G.M., 1992. Near-limit drop deformation and secondary breakup. Int. J. Multiphase Flow 18, 635–652.
Hsiang, L.P., Faeth, G.M., 1993. Drop properties after secondary breakup. Int. J. Multiphase Flow 19, 721–735.
Hsiang, L.P., Faeth, G.M., 1995. Drop deformation and breakup due to shock wave and steady disturbances. Int. J. Multiphase Flow 21, 545–560.
Hwang, S.S., Liu, Z., Reitz, R.D., 1996. Breakup mechanisms and drag coefficients of high-speed vaporizing liquid drops. Atomization Sprays 6, 353–376.
Katz, J., Sheng, J., 2010. Applications of holography in fluid mechanics and particle dynamics. Annu. Rev. Fluid Mech. 42, 531–555.
Kékesi, T., Amberg, G., Prahl Wittberg, L., 2014. Drop deformation and breakup. Int. J. Multiphase Flow 66, 1–10.
Kline, S., McClintock, F., 1953. Describing uncertainties in single-sample experiments. Mech. Eng. 75, 3–8.
Komabayasi, M., Gonda, T., Isono, K., 1964. Life time of water drops before breaking and size distribution of fragment droplets. J. Meteorol. Soc. Jpn. 42, 330–340.
Kulkarni, V., Guildenbecher, D.R., Sojka, P.E., 2012. Secondary atomization of Newtonian liquids in the bag breakup regime: comparison of model predictions to experimental data. ICLASS 2012, 12th International Conference on Liquid Atomization and Spray Systems. Heidelberg, Germany.
Kulkarni, V., Sojka, P.E., 2014. Bag breakup of low viscosity drops in the presence of a continuous air jet. Phys. Fluids 26, 072103.
Lamb, H., 1916. Hydrodynamics. Cambridge University Press, London.
Lane, W.R., 1951. Shatter of drops in streams of air. Ind. Eng. Chem. 43, 1312–1317.
Li, X., Tankin, R.S., 1987. Droplet size distribution: a derivation of a Nukiyama-Tanasawa type distribution function. Combust. Sci. Technol. 56, 65–76.
Linne, M., 2013. Imaging in the optically dense regions of a spray: a review of developing techniques. Prog. Energy Combust. Sci. 39, 403–440.
Liu, Z., Reitz, R.D., 1997. An analysis of the distortion and breakup mechanisms of high speed liquid drops. Int. J. Multiphase Flow 23, 631–650.
Lu, J., Fugal, J.,P., Nordsiek, H., Saw, E.W., Shaw, R.,A., Yang, W., 2008. Lagrangian particle tracking in three dimensions via single-camera in-line digital holography. New J. Phys. 10, 125013.
Masliyah, J.H., Epstein, N., 1970. Numerical study of steady flow past spheroids. J. Fluid Mech. 44, 493–512.
O'Rourke, P.J., Amsden, A.A., 1987. The TAB method for numerical calculation of spray droplet breakup. International Fuels and Lubricants Meeting and Exposition. SAE Technical Paper Services. Toronto, Ontario.
Pilch, M., Erdman, C.A., 1987. Use of breakup time data and velocity history data to predict the maximum size of stable fragments for acceleration-induced breakup of a liquid drop. Int. J. Multiphase Flow 13, 741–757.
Quan, S., Lou, J., Schmidt, D.P., 2009a. Modeling merging and breakup in the moving mesh interface tracking method for multiphase flow simulations. J. Comput. Phys. 228, 2660–2675.
Quan, S., Schmidt, D.P., Hua, J., Lou, J., 2009b. A numerical study of the relaxation and breakup of an elongated drop in a viscous liquid. J. Fluid Mech. 640, 235–264.
Quan, S.P., Schmidt, D.P., 2006. Direct numerical study of a liquid droplet impulsively accelerated by gaseous flow. Phys. Fluids 18, 9.
Reitz, R.D., 1987. Modeling atomization processes in high-pressure vaporizing sprays. Atomization Spray Technol 3, 307–337.
Schnars, U., Jueptner, W., 2005. Digital Holography: Digital Hologram Recording, Numerical Reconstruction, and Related Techniques. Springer, Berlin.
Sellens, R., Brzustowski, T., 1985. A prediction of the drop size distribution in a spray from first principles. Atomization Spray Technol. 1, 89–102.
Simmons, H.C., 1977. The correlaiton of drop-size cistributions in fuel nozzle sprays part 1: the drop-size/volume-fraction distribution. J. Eng. Power 309–314.
Soria, J., Atkinson, C., 2008. Towards 3C-3D digital holographic fluid velocity vector field measurement—tomographic digital holographic PIV (Tomo-HPIV). Meas. Sci. Technol. 19, 074002.
Tani, S., Tanaka, Y., Murata, S., 2015. Measurement of three-dimensional particle distribution by tomographic digital holography. ASME-JSME-KSME 2015 Joint Fluids Engineering Conference. Seoul, Korea.
Taylor, G., 1950. The instability of liquid surfaces when accelerated in a direction perpendicular to their planes. I.. Proc. R. Soc. London, Ser. A 201, 192–196.
Taylor, G.I., 1963. The shape and acceleration of a drop in a high-speed air stream. In: Batchelor, G. (Ed.), The Scientific Papers of GI Taylor. University Press, Cambridge.
Theofanous, T.G., 2011. Aerobreakup of Newtonian and viscoelastic liquids. Annu. Rev. Fluid Mech. 43, 661–690.
Tinevez, J.-Y., 2012. Simple Tracker http://www.mathworks.com/matlabcentral/fileexchange/34040-simple-tracker.
Tryggvason, G., 1997. Computational Investigation of Atomization ARL-SR-BL-TR-98.
Wadhwa, A.R., Magi, V., Abraham, J., 2005. Hybrid compressible-incompressible numerical method for transient drop-gas flows. AIAA J 43, 1974–1983.
Wadhwa, A.R., Magi, V., Abraham, J., 2007. Transient deformation and drag of decelerating drops in axisymmetric flows. Phys. Fluids 19, 20.
Wu, Y., Wu, X., Yao, L., Brunel, M., Coëtmellec, S., Lebrun, D., Gréhan, G., Cen, K., 2016. 3D boundary line measurement of irregular particle with digital holography. Powder Technology 295, 96–103.